Nuclear Instruments and Methods in Physics Research A 653 (2011) 35–41

Contents lists available at ScienceDirect

Nuclear Instruments and Methods in Physics Research A

journal homepage: www.elsevier.com/locate/nima

Fast electron generation using PW-class PEARL facility

A.A. Soloviev *, K.F. Burdonov, V.N. Ginzburg, A.A. Gonoskov, E.V. Katin, A.V. Kim, A.V. Kirsanov, A.V. Korzhimanov, I.Yu. Kostyukov, V.V. Lozhkarev, G.A. Luchinin, A.N. Mal'shakov, M.A. Martyanov, E.N. Nerush, O.V. Palashov, A.K. Poteomkin, A.M. Sergeev, A.A. Shaykin, M.V. Starodubtsev, I.V. Yakovlev, V.V. Zelenogorsky, E.A. Khazanov

Institute of Applied Physics, Russian Academy of Sciences, 46 Ulyanov st., Nizhny Novgorod 603950, Russia

ARTICLE INFO

Available online 12 March 2011

Keywords:
PW-laser
Laser–plasma interaction
Wake-field generation
Bubble regime
GeV-range electron beams

ABSTRACT

We use a PW-class PEARL facility to study fast electron beam generation during high intensity laser pulse interaction with a supersonic gas jet. We show that electron beams with several hundreds of MeV and relatively large charges, of hundreds of pC and more, can be effectively produced without any guiding structures. PIC simulations also confirm the obtained experimental data and provide optimized conditions of laser–plasma interaction for high-charged beam production.

© 2011 Elsevier B.V. All rights reserved.

1. Introduction

Recent advances in the high-power laser technology have stimulated a growing number of laboratories around the world to develop table-top multiterawatt and petawatt-class laser facilities. Among the consequences of such developments are major breakthroughs [1] in the field of electron acceleration via the laser wakefield accelerator (LWFA) concept [2]. In this case electrons surf the electric fields exceeding 100 GV/m, which is more than 1000 times stronger than the values achievable in conventional accelerators. These fields are generated within plasma structures in the form of plasma waves or electron density "bubbles" [3] propagating at near-light speed behind laser pulses [4–6].

In the current paper we present the results of electron acceleration using high intensity laser pulses from the PW level PEARL (PEtawatt pARametrical Laser) facility interacting with a gas jet. To the best of our knowledge, this is the first petawatt-class laser employing the OPCPA technology. The PEARL facility produces in the normal operating mode 60 fs laser pulses at a wavelength of 910 nm and energy up to 10 J (in the optimized operating mode the pulse energy is 25 J with a duration of 45 fs [7]). We have studied theparameters of the generated electron beam as a function of the conditions of laser–plasma interaction, such as plasma density, interaction length, focusing angle, and others. These experiments are also supported by the particle-in-cell (PIC) simulation.

The paper is organized as follows. In Section 2 we consider the layout of the electron acceleration facility and experimental diagnostics used to measure laser, gas jet and plasma parameters. Experimental results of GeV-class electron beam generation are presented in Section 3. In Section 4 simulation of laser interaction with under-dense plasma relevant to the conducted experiments and their correspondence are analyzed. Finally, Section 5 contains discussion of the results obtained.

2. Experimental setup and diagnostics

The experimental setup is illustrated schematically in Fig. 1. The main PEARL pulse after compressor is split into two parts. The powerful pulse then serves as a driver coming after the compressor into the target chamber where it is focused into a supersonic gas jet by means of an off-axis parabolic mirror with f/15 or f/6 forming the focal spot sizes of the laser beam of 18 and 7.2 μm at FWHM intensity, respectively. The average laser intensities correspond to the normalized vector potential $a_0=2$ and 7, respectively. The second part with a much lower power transmitted by the mirror m_1 arrives at the diagnostic channel where it is used for monitoring the driver and for the interferometric diagnostics of plasma density (see below). It should be noted that Thomson scattering in the direction normal to the driving pulse polarization, which is not shown in Fig. 1, has also been measured. The gas (helium and nitrogen) jet is formed with a specially designed supersonic conical nozzle having diameters 2, 5, and 10 mm. The gas nozzles are calibrated by the Michelson interferometer in one arm of which the gas jet is placed. The interference patterns are registered by a CCD camera. The inverse Abel transformation

* Corresponding author.
E-mail address: so_lo@appl.sci-nnov.ru (A.A. Soloviev).

0168-9002/$ - see front matter © 2011 Elsevier B.V. All rights reserved.
doi:10.1016/j.nima.2011.01.180

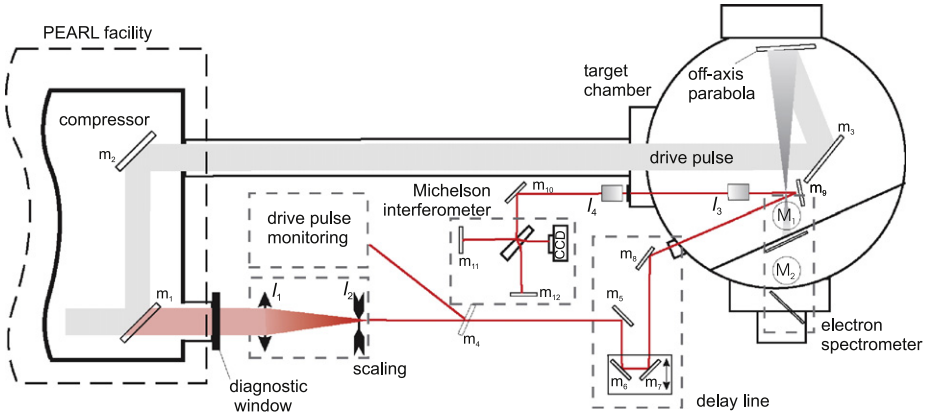

Fig. 1. (Color online) Experimental LWFA complex at PEARL facility: m_1–m_{12} are mirrors, l_1–l_4 are lenses, M_1–M_2 are magnets.

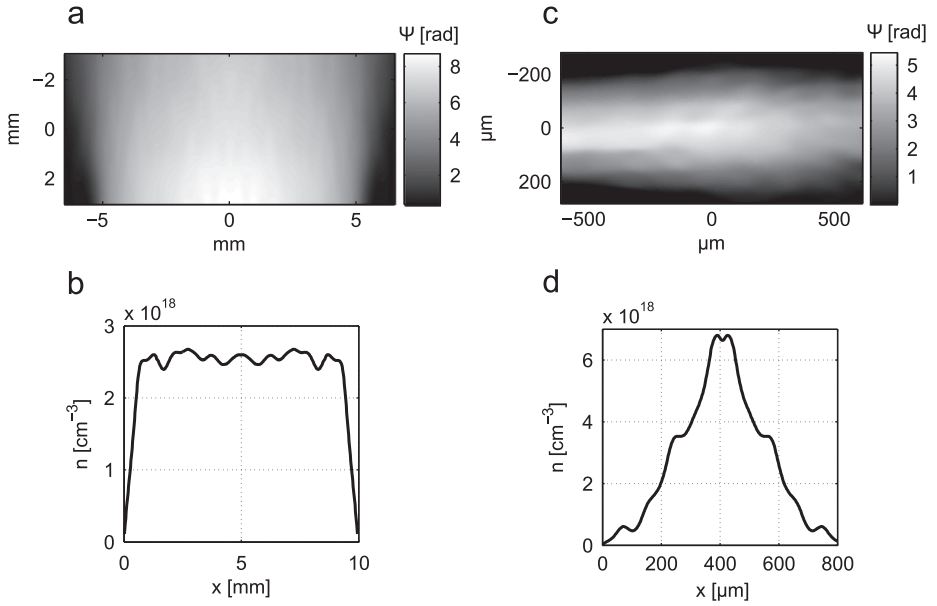

Fig. 2. Nitrogen jet induced phase distortions (a) and corresponding neutral density profile (b) for 10 mm nozzle at 100 bar of backing pressure; typical plasma channel phase distortions (c) and corresponding plasma density profile (d) for 10 mm nozzle and 30 bars of nitrogen backing pressure.

is also applied to the gas jet induced phase distortions to reconstruct the gas density profile. The calibration shows that the nozzles produce flat-top gas density profiles with a plateau size of 1, 3.5 and 8 mm for the 2, 5 and 10 mm diameter nozzles, respectively. A typical jet induced phase distortion and density profile at 1 mm above the nozzle edge for the 10 mm gas jet are presented in Fig. 2(a) and (b). The calibration shows that the value of gas density depends linearly on the nozzle backing pressure for the range of 5–100 bar.

Direct measuring of plasma density by means of the Michelson interferometer was performed (see Fig. 1). The probe radiation that is a weaker femtosecond replica of the high-power pulse allows temporal resolution of the phase measurements on a femtosecond time scale. It should be noted that using this technique plasma density distribution can be measured correctly, if the plasma channel has axial symmetry. In fact, in a He gas jet the measured plasma density exceeds neutral density by a factor of 2, which means that He is fully ionized. This is in a good agreement with the fact that at the laser intensities of order 10^{19} W/cm^2 used in the experiment He gas should be fully ionized [9]. However, for N_2 gas jet the ionization degree depends on laser intensity and, hence, the plasma channel is strongly nonuniform in radial direction. Full ionization of nitrogen occurs only at laser intensities exceeding 10^{19} W/cm^2 [10]. According to this paper we expect five times ionized nitrogen for the focusing angle f/15 and fully stripped nitrogen plasma in experiment with f/6 focusing mirror. The resulting observations are presented in Fig. 2(c) and (d). One can see a plasma channel with the corresponding plasma density $N_e = 7 \times 10^{18}$ cm^{-3} measured at 30 bar backing pressure and f/15 focusing.

Table 1
Gas density and the corresponding plasma density for backing pressure of 10 bar.

Nozzle diameter (mm)	N/N_e, 10^{18} cm^{-3}, He	N/N_e(f/6)/N_e(f/15), 10^{18} cm^{-3}, N_2
2	1.8/3.6	1.8/25/18
5	1.75/3.5	1.5/21/15
10	0.25/0.5	0.25/3.5/2.5

The neutral density N and the corresponding plasma density N_e for different nozzles at 10 bar backing pressure are given in Table 1.

To measure the high intensity laser–plasma interaction region we have used a diagnostic method based on the observation of

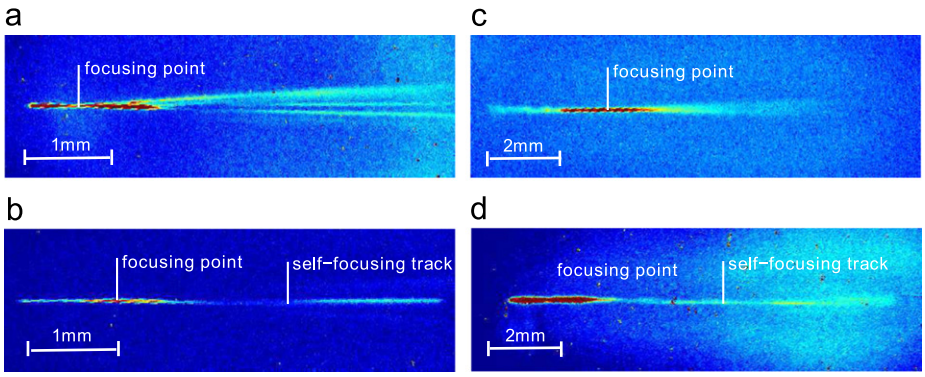

Fig. 3. (Color online) Image of Thomson-scattered light at the second harmonic of laser radiation in the direction normal to the polarization plane.

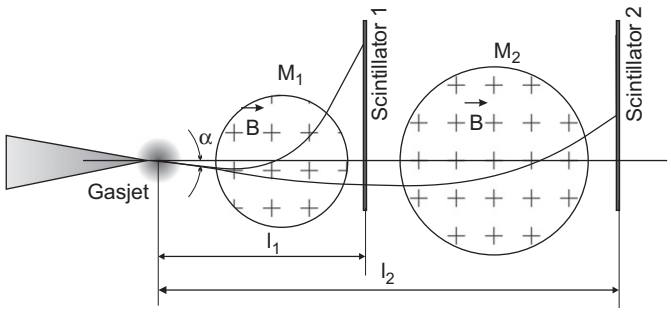

Fig. 4. Schematic diagram of electron energy spectrometer.

Thomson scattering at the second harmonic of laser radiation. Typical side-view images of the scattered light are presented in Fig. 3 for the 5 mm nozzle (a, b) and for the 10 mm nozzle (c, d). The driver pulse is coming from the left. One can see that Thomson scattering is observed from a long narrow trace with characteristic length of the order of gas jet diameter (Fig. 3(b) and (d)). This fact confirms self-channeling of the pump laser beam due to relativistic nonlinearity. In some cases no self-focusing is observed (c) and one can see cones of geometrical divergence. If the focusing point is a little ahead of the homogenous area of the gas jet, a multichannel structure can be observed (a). We have not found any significant positive correlation between the appearance of long traces in Thomson scattering picture and the appearance of monoenergetic electron beams or their energy. Indeed, high-energy electron beams are not accompanied by long traces as a rule. The relationship between Thomson scattering and high-energy electron beams generation needs additional study.

The most important measurement technique used is an electron energy spectrometer. We employ two scintillation screens (instead of one), which greatly increases accuracy of electron energy spectrum measurements. The schematic diagram of this spectrometer is shown in Fig. 4. Lengths l_1 and l_2 were 15 and 40 cm, respectively. The characteristic magnetic field amplitude and diameter for magnets M_1 and M_2 were, correspondingly, 0.45 and 0.7 T × 6 cm. This spectrometer allows measuring in a single shot simultaneously the energy and angular spectra of a narrow electron beam without any assumption about value of its injection angle α (Fig. 4). The scintillating screens had absolute calibration [11], which allows finding the charge of a narrow electron beam to an accuracy up to 0.5 pC. The details of the spectrometer and methods of narrow electron beam spectrum reconstruction are discussed in Ref. [12]. Moreover, in Ref. [12] the effect of small-angle electron scattering in the bulk of the first scintillator is assessed theoretically and measured in the experiments. It is shown that the electron beams with energy higher than 200 MeV may be measured to a high accuracy if this effect is neglected.

The spectral measurements accuracy strongly depends on the accuracy of placing the scintillator screens. A simple method of enhancing placement accuracy by means of an optical reference point is proposed. The method is based on using a small part of pump PW laser radiation passing through the small aperture in the first scintillator so as to take into account mutual transverse displacement of the scintillators. The brightness of the optical reference can be interpreted as an indicator of laser–plasma interaction. For example, in case of self-focusing, the size of the focal spot becomes smaller and the driver pulse geometrical divergence increases. Thus, the laser intensity in the plane of the first scintillator as well as optical reference intensity subside.

The use of a single-shot electron spectrometer with two scintillators and optical reference allows reaching an accuracy better than 8% for $W=270$ MeV beam with energy spread $\Delta W = 30$ MeV. Such an accuracy is obtained for a 40 cm long spectrometer with 0.7 T × 9 cm constant-magnet system. The use of the described spectrometer scheme enhances significantly measurement accuracy of electron spectra as compared to a single-scintillator spectrometer with similar size and magnetic field.

3. GeV-range electron beam generation

Using f/6 and f/15 optics we have performed a parametric scan for efficient electron beam generation over a wide range of gas jet densities from 1×10^{18} to 1.2×10^{19} cm^{-3}. The pulse duration was within 50–70 fs. The normalized vector potential a_0 in the focusing region was within 1–2.5 for f/15, and 5–9 for sharp focusing f/6. Accelerated electron beams were observed only above the threshold $P/P_c \geq 2$, where $P_c = 17(N_c/N_e)^{1/2}$ GW, $N_c \approx 1.3\times10^{21}$ cm^{-3} is the critical plasma density. The threshold character of the electron beams generation was observed in the work [13] as well. No apparent dependence of electron beams on parameter a_0 and duration in particular was observed above this threshold.

No electron beams were observed at shots into low-density plasma ($P/P_c < 2$), and the optical reference intensity was close to the intensity in the absence of a gas jet.

When the plasma density exceeded the threshold of about $P/P_c=2$, the optical reference brightness dropped abruptly and there appeared unit electron beams with the angular size of 5–10 mrad and energies of 80–300 MeV. The angle of flight of the unit beams could differ from shot to shot, but it was always within the angle of focusing. The charge of the unit beams in the experiments reached 300 pC. A typical image of a narrow electron

beam in the plane of the second scintillator is presented in Fig. 5(c). According to Ref. [3], the plasma wave excitation is most effective when the laser pulse is shorter than the plasma wavelength $\lambda_p = 2\pi c a_0^{1/2}/\omega_p$ and fits completely into the first half of the plasma wave:

$$L = \lambda_p/2. \quad (1)$$

In our case, the longitudinal size $L = c \times 60\ \text{fs} \approx 20\ \mu\text{m}$ of the optical pulse is the largest one. For the considered intensities the condition (1) is fulfiled with the density $N_e = 1.5 \times 10^{18}\ \text{cm}^{-3}$ for the parabola f/15 and with $N_e = 5 \times 10^{18}\ \text{cm}^{-3}$ for f/6. The most energetic electron beams were observed in the vicinity of these values.

A further increase of the plasma density, and hence of P/P_c, resulted in space-time inhomogeneity and splitting of the optical pulse into smaller fractions. Some of these fractions may serve as drivers for their electron beams [14]. The electron beams comprising two or more beams will be referred to as clusterized ones. A typical picture of a clusterized beam in the plane of the second scintillator is shown in Fig. 5(b). If the cluster shape on the first scintillator was similar to that on the second one, then it was possible to measure the mean cluster energy, even if the cluster was off-axis. This is the advantage of the used spectrometer as compared to the slot spectrometer employed, for example, in the work [15], in which the output angular spectrum of electrons is forced to narrow. Note that the cluster energy is usually lower and the angular size larger than in the unit beams.

In shots into a denser plasma, clusters grew in number and started to overlap, eventually resulting in the formation of electron beams with a wide angular and energy spectra (Fig. 5(a)). The maximum electron energy in such beams was of the order of several hundreds of MeV. It was a lower estimate obtained at an angle equal to a half focusing angle (see Fig. 4). We could not assess more precisely the energy of the electron beam, as our spectrometer does not allow high-accuracy measurement in the case of a wide angular spectrum.

The qualitative picture described above may be supplemented by the following plots. The dependence of the angular size (FWHM) and average cluster energy on plasma density is plotted in Fig. 6(a) and (b) for a 10 mm nozzle and f/15 focusing. The obvious tendency is an increase in energy and diminution of

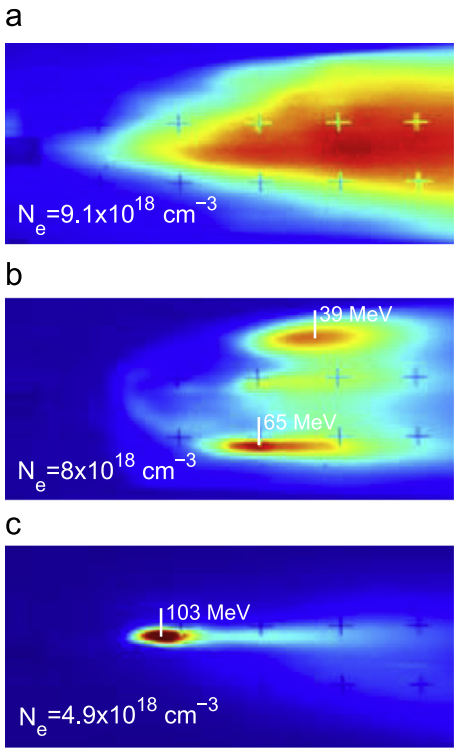

Fig. 5. (Color online) Electron beams of different types in the plane of the second scintillator: wide beam (a), clustered beam (b), narrow quasi-monoenergetic beam (c). Electrons are deflected by the magnetic field to the right.

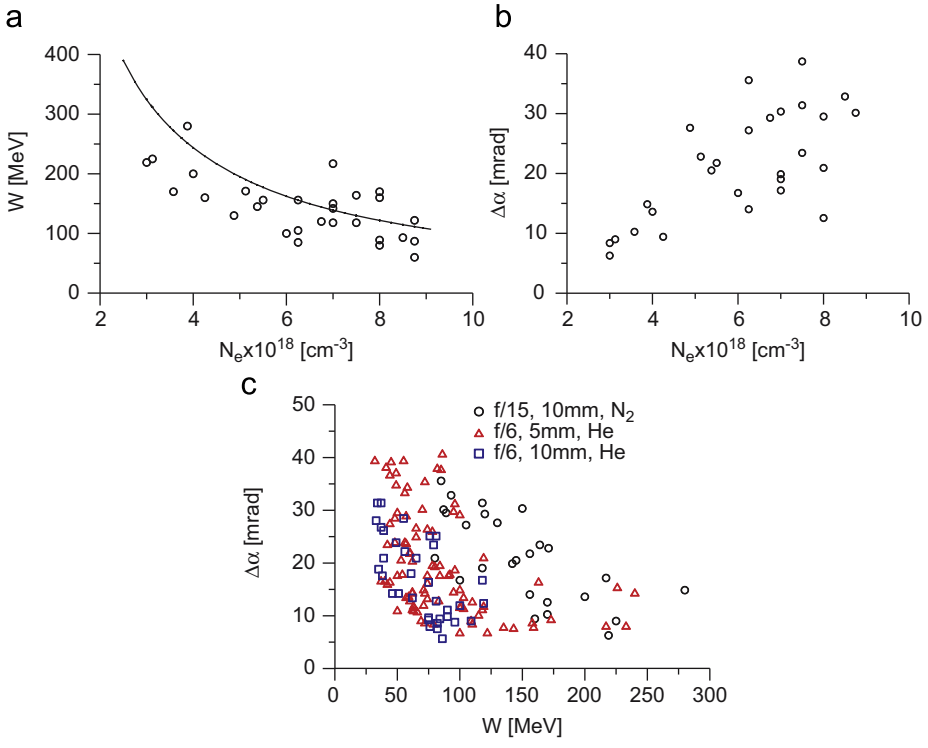

Fig. 6. Relationships between energy W, plasma density N_e and angular size $\triangle\alpha$ of experimental electron beams. The solid line depicts the theoretical estimates for W_{max}.

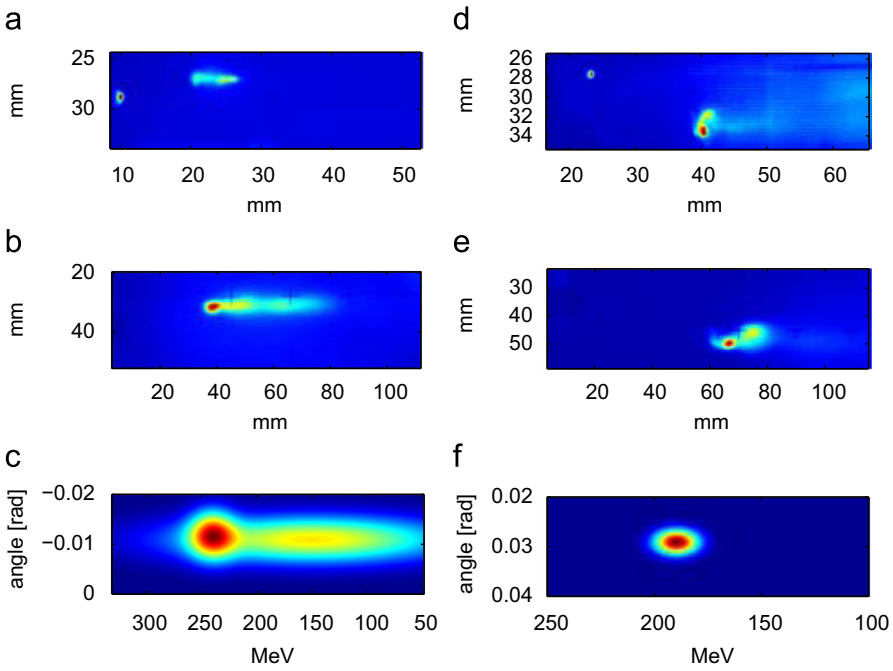

Fig. 7. (Color online) Experimental luminescence of scintillators for two different beams. The first beam with 270 MeV peak energy is presented in (a) and (b) for the first and the second scintillator, respectively. The second 190 MeV beam is presented in (c) and (d) for the first and the second scintillator, respectively. The corresponding model spectrum (c, f).

cluster size with decreasing pressure. The minimal size of the cluster versus its energy is plotted in Fig. 6(c) for f/15 focusing and 10 mm nozzle (circles), f/6 focusing and 10 mm nozzle (triangles), and f/6 focusing and 6 mm nozzle (squares). Independent of focusing, more energetic clusters have a smaller angular size. The increase of electron beam energy with plasma density decrease is in agreement with the phenomenological theory of acceleration in the "bubble" regime described in Ref. [8]. According to Ref. [8] the maximum electron beam energy W_{max} for given N_e and a_0 can be estimated to be $W_{max} \approx (2/3)mc^2(N_e/N_c)a_0$, where mc^2 is the electron rest energy. Good agreement is seen in Fig. 6(a), where we depicted a series of experimental measurements of beam energy and the corresponding theoretical estimates.

Let us now address the energy spectrum of separate electron beams. First, in Fig. 7 one can see the experimental luminescence from the first (a, d) and the second (b, e) scintillators for two different electron beams (the first beam in Fig. 7(a) and (b); the second beam in Fig. 7(d) and (e)). The electrons are deflected by the magnetic field to the right. The procedure of energy spectrum reconstruction from the luminescence of both screens is described in detail in Ref. [12]. This procedure consists in minimizing the difference between the Monte-Carlo simulated luminescence of the model electron beam and the experimental luminescence. The simulated luminescence is found via single electron trajectory calculations. The reconstructed electron beams spectra are presented in Fig. 7(c) and (f) for the first and the second beam, respectively.

For the first beam with $W=270$ MeV and $\Delta W = 30$ MeV this approach gives an accuracy of ± 20 MeV for the mean energy and of ± 10 MeV for the energy spread. It is one of the most energetic beams obtained in the experiments. The second beam with $W=190$ MeV has one of the most narrow experimental energy spreads $\Delta W = 8$ MeV.

The charges of the electron beams depicted in Fig. 7 are equal to 18 and 11 pC for the first and the second beam, respectively. The charge of the quasi-monoenergetic electron beams obtained in experiment amounted at least up to 300 pC.

4. Simulation

To analyze the mechanism of electron acceleration observed in the experiments we performed a series of 3D PIC simulations with parameters close to the experimental ones. We simulated the process of the entrance and further propagation of a linearly polarized laser pulse in a plasma with a sharp boundary and the electron density of 5×10^{18} cm^{-3}. The initial laser pulse with the wavelength of 0.91 μm and the total energy of E at the input to plasma had a flat phase front and a Gaussian profile with size D (FWHM in intensity) in the transverse direction and $c\tau$ in the longitudinal direction. The pulse propagation was simulated using the technique of a pulse co-moving simulation window having size 80 μm × 64 μm × 64 μm which was represented by $1024 \times 256 \times 256$ cells. In an unperturbed plasma state, each cell contained on the average four virtual particles of each type, and a plasma oscillation period was represented by 256 time steps. A parallel FFT based PIC code ELMIS was used for the simulations [16]. An important feature of this code is exact fulfilment of the dispersion relation for all electromagnetic waves in vacuum whose spatial period is resolved by two cells at least. This circumstance is especially important at long acceleration distances.

As was to be expected for the considered parameters, the simulation showed a strongly nonlinear mode, when a wakefield breaks and a structure in the form of several bubbles following one after another is formed. Two stages of this process may be distinguished: formation of a stable structure when a complex nonlinear process of pulse compression in the transverse directions occurs and stable pulse propagation. The electrons are entrapped into accelerating phase in the transition from the first to the second mode. The simulation shows trapping of at least three individual electron beams, two of which are entrapped with a small interval by the leading bubble, and one, less energetic beam by the second bubble. Formation of further bubbles and further electron trapping may evidently be also observed, but our computations were restricted by the size of the simulation box. The evolution of electron energy distribution is illustrated

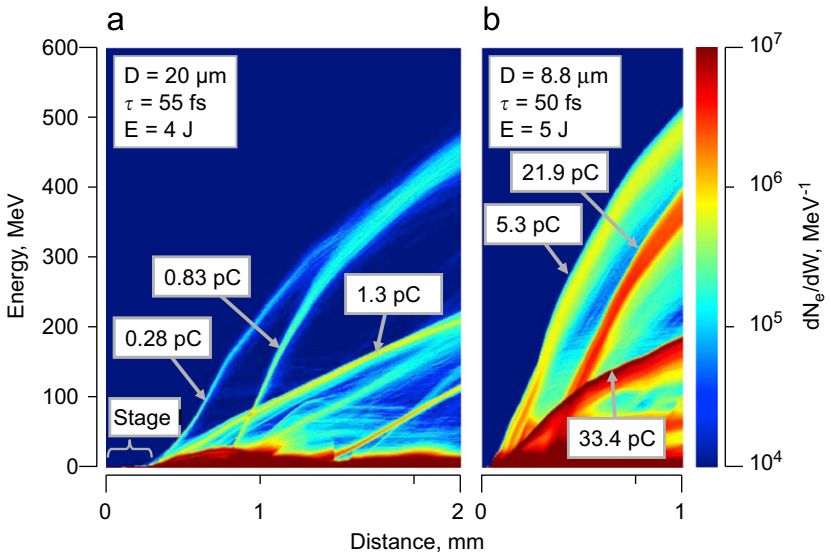

Fig. 8. (Color online) Energy distribution of electrons as a function of acceleration distance.

in Fig. 8. In the leading bubble structure, the electrons are accelerated up to energies of order 500 MeV already at a 2 mm distance, but the electron beam contains a relatively small charge from 0.2 to 5 pC; whereas in the second bubble structure acceleration up to 200 MeV occurs at the same distance, but a much larger charge of several tens of pC is entrapped. Typical values of the experimental beam energy and charge are in a good agreement with the parameters of the electron beams accelerated by the second bubble structure. The lack of knowledge of the laser pulse field structure does not allow more detailed comparison.

Electron acceleration in a strongly nonlinear mode observed at rather high laser pulse amplitudes is known to have the following features. First, a laser pulse propagating in plasma may be subject to self-compression and subsequent self-channeling, thus enabling propagation over distances much longer than the Rayleigh length. Second, on attaining a threshold amplitude in the self-channeling mode the wakefield breaks and the electric field structure suitable for stable acceleration of the electron beam is formed behind the laser pulse. Third, any inhomogeneities in plasma lead to fluctuations of the structure and electron trapping from plasma to accelerating phase. Thus, unlike the linear mode of electron acceleration, both problems, pulse channeling and electron loading are solved, ensuring relative simplicity of staging the experiment. On the other hand, however, there are no direct mechanisms of controlling the process of electron loading, because it strongly depends on plasma inhomogeneities that are encountered on the laser pulse path at stable self-channeling. As powerful laser pulses are usually rather unstable, the instant and amount of the entrapped electrons have low recurrence.

For determining how the number of the entrapped electrons is sensitive to the conditions of trapping we conducted two numerical experiments. In the first of them the initial pulse had the transverse size $D=20$ μm and was first compressed down to a stable mode (Fig. 8(a)). In the second experiment the laser pulse had the shape corresponding to the stable propagation mode already at the entrance to the plasma (Fig. 8(b)). It is clear from Fig. 8 that at least three electron beams are entrapped and gain energy with increasing propagation path identically in the two numerical experiments. However, in the first case, entrapping occurs when the phase of laser pulse compression (shown as "stage I" in Fig. 8) is over; whereas in the second case it takes place immediately at the entrance to plasma. It is interesting that the amount of the entrapped electrons is more than 10 times larger in the second case due to the sharp plasma boundary, which indicates a high sensitivity of the number of entrapped particles to the amplitude of the inhomogeneities passed by the laser pulse in a stable mode.

5. Conclusion

The LWFA complex has been created on the basis of the PEARL facility that generates, in different shots, quasi-monoenergetic electron beams with energies up to 300 MeV, minimum angular size of 6 mrad FWHM, and charge as large as 300 pC. In view of relatively low stability of parameters of laser radiation much attention was focused on measuring parameters of each LWFA. Conical supersonic gas nozzles producing homogeneous distribution of gas with characteristic size 1, 3, 5, and 8 mm were developed and optically calibrated. Direct interferometric diagnostics of plasma density was done. To increase accuracy of measuring accelerated electron beam spectra a two-screen constant-magnet spectrometer was employed [12]. The spectrometer allows simultaneous finding of the angular and energy spectra of each electron beam. The measurement accuracy greatly exceeds that of a one-screen spectrometer with analogous size and magnetic field. Electron beams were observed above the threshold $P/P_c > 2$. Qualitative dependence of the behaviour of the generated beams on plasma density has been considered. For the focusing angle f/15, experiments demonstrated a tendency to electron beam energy increase with decreasing plasma density in the 9×10^{18}– 1.2×10^{18} cm^{-3} range. This dependence is in a good agreement with the phenomenological theory described in Ref. [8]. It was demonstrated in experiments that the angular size of the electron beams decreases with the increase of their mean energy for helium and nitrogen jets 5 and 10 mm in diameter.

The performed numerical simulations show that, for the parameters of the considered experiments, the electrons are entrapped and accelerated in the bubble mode. The first bubble structure 500 MeV at 2 mm distance, whereas their total charge varies from 0.2 to 5 pC, depending on the conditions of trapping. At the same time the electron beams accelerated by the second bubble structure approach energies of about 300 MeV and have a

few tens of pC charge, which agrees well with typical values obtained in the experiments.

Acknowledgments

This research was supported by the Presidium of RAS, the RFBR (Grants No. 09-02-12322-ofi_m, 11-02-01070-a, 10-02-00982-a), the Presidential Council on Grants of the Russian Federation (Grant No. 3800.2010.2) and the Ministry of Education and Science of the Russian Federation (contract No. 02.740.11.0225). We acknowledge the Joint Supercomputer Center of RAS and the Swedish National Infrastructure for Computing (SNIC) for the provided supercomputer sources.

References

[1] C.E. Clayton, et al., Phys. Rev. Lett. 105 (2010) 105003.
[2] T. Tajima, J.M. Dawson, Phys. Rev. Lett. 43 (1979) 267.
[3] A. Pukhov, J. Meyer-ter Vehn, Appl. Phys. B 74 (2002) 355.
[4] C. Geddes, et al., Nature 431 (2004) 538.
[5] S. Mangles, et al., Nature 431 (2004) 535.
[6] J. Faure, et al., Nature 431 (2004) 541.
[7] V. Lozhkarev, et al., Laser Phys. Lett. 4 (6) (2007) 421.
[8] W. Lu, et al., Phys. Rev. Spec. Top. Acceler. Beams 10 (2007) 061301.
[9] B. Walker, et al., Phys. Rev. A 48 (1993) R894.
[10] S. Hulin, et al., Phys. Rev. E 61 (2000) 5693.
[11] Y. Glinec, et al., Rev. Sci. Instrum. 77 (2006) 103301.
[12] A. Soloviev, E. Khazanov, Proc. SPIE 7751 (2010) 77511G.
[13] D.H. Froula, et al., Phys. Rev. Lett. 103 (2009) 215006.
[14] B. Hidding, et al., Phys. Plasmas 16 (2009) 043105.
[15] S. Kneip, et al., Phys. Rev. Lett. 103 (2009) 035002.
[16] 〈www.ipfran.ru/english/structure/lab334/simlight.html〉.